



HAL
open science

Thermal boundary conductance of CVD-grown MoS₂ monolayer-on-silica substrate determined by scanning thermal microscopy

Christian Mateo Frausto-Avila, Victor Arellano-Arreola, Jose Martin Yañez Limon, Andres de Luna-Bugallo, Séverine Gomès, Pierre-Olivier Chapuis

► **To cite this version:**

Christian Mateo Frausto-Avila, Victor Arellano-Arreola, Jose Martin Yañez Limon, Andres de Luna-Bugallo, Séverine Gomès, et al.. Thermal boundary conductance of CVD-grown MoS₂ monolayer-on-silica substrate determined by scanning thermal microscopy. *Applied Physics Letters*, 2022, 120 (26), pp.262202. 10.1063/5.0092553 . hal-03740535

HAL Id: hal-03740535

<https://hal.science/hal-03740535v1>

Submitted on 29 Jul 2022

HAL is a multi-disciplinary open access archive for the deposit and dissemination of scientific research documents, whether they are published or not. The documents may come from teaching and research institutions in France or abroad, or from public or private research centers.

L'archive ouverte pluridisciplinaire **HAL**, est destinée au dépôt et à la diffusion de documents scientifiques de niveau recherche, publiés ou non, émanant des établissements d'enseignement et de recherche français ou étrangers, des laboratoires publics ou privés.

Thermal boundary conductance of CVD-grown MoS₂ monolayer-on-silica substrate determined by scanning thermal microscopy

C.M. Frausto-Avila^{a,b}, V. Arellano-Arreola^b, J.M. Yañez-Limon^b, A. De Luna-Bugallo^{b,c,*}, S. Gomès^a, P.-O. Chapuis^{a,*}

^a Univ Lyon, CNRS, INSA-Lyon, Université Claude Bernard Lyon 1, CETHIL UMR5008, F-69621, Villeurbanne, France

^b Cinvestav Unidad Querétaro, Querétaro, Qro. 76230, Mexico

^c Departamento de Nanotecnología, Centro de Física Aplicada y Tecnología Avanzada, Universidad Nacional Autónoma de México, CP 76000, Querétaro, Qro., Mexico.

*Corresponding authors: aluna@fata.unam.mx, olivier.chapuis@insa-lyon.fr

We characterize heat dissipation of supported MoS₂ monolayers grown by chemical vapour deposition (CVD) by means of ambient-condition scanning thermal microscopy (SThM). We find that the thermal boundary conductance of the MoS₂ monolayers in contact with 300 nm of SiO₂ is around $4.6 \pm 2 \text{ MW}\cdot\text{m}^{-2}\cdot\text{K}^{-1}$. This value is in the low range of the values determined for exfoliated flakes with other techniques such as Raman thermometry, which span an order of magnitude ($0.44 - 50 \text{ MW}\cdot\text{m}^{-2}\cdot\text{K}^{-1}$) and underlines the dispersion of the measurements. The sensitivity to the in-plane thermal conductivity of supported MoS₂ is very low, highlighting that the thermal boundary conductance is the key driver of heat dissipation for the MoS₂ monolayer when it is not suspended. In addition, this work also demonstrates that SThM calibration using different thicknesses of SiO₂, generally employed in bulk materials, can be extended to 2D materials.

Over the last two decades, there has been a growing interest in 2D materials due to their low dimensionality, making them attractive for various fields such as electronics, condensed matter, photonics, catalysis, among others. After the popularization of graphene, different layered materials have been discovered, including borophene¹, hexagonal boron nitride hBN², and transition metal dichalcogenides³ (TMDCs). Molybdenum disulfide (MoS₂), a member of the family of TMDCs, is a semiconductor whose synthesis has been quite well developed and established by different approaches⁴⁻⁹. In the case of a single layer (thickness around 6 Å) MoS₂ exhibits a direct bandgap¹⁰ ($\approx 1.82 \text{ eV}$), reasonable electrical conductivity, large spin-orbit coupling, strong exciton binding, which makes it suitable for several optoelectronic applications^{11,12}.

Investigating the properties of 2D materials and implementing various characterization techniques are challenging in many cases, particularly for thermal studies, due to the complexity associated with their extremely-low thickness. With the advent of atomically thin materials, different thermal characterization techniques have been extrapolated from bulk to nanostructured materials. Techniques such as the 3ω method¹³, photothermal characterization¹⁴, as well as Raman thermometry¹⁵, have been efficiently translated for thermal conductivity measurements of such materials. Some of the techniques require depositing metallic contacts onto the samples¹⁶, which is unfeasible for certain configurations of the systems, or high-frequency equipment¹⁷ with assumptions on the (ideal) optical absorption.

Thermal characterization aims mainly at obtaining parameters such as thermal conductivity and thermal boundary conductances (TBCs). Due to the quick preparation and crystal quality, most of the reports

regarding the thermal properties of MoS₂ are normally performed using exfoliated samples (either supported by an arbitrary substrate or suspended in a micrometer-sized hole), however MoS₂ crystals can also be grown by chemical vapor deposition (CVD), which appears more appropriate for device integration and scaling¹⁸. For supported exfoliated monolayers (flakes), thermal conductivity values in the range $34.5\text{-}62.0 \text{ W}\cdot\text{m}^{-1}\cdot\text{K}^{-1}$ are reported, while TBCs span $0.44\text{-}50 \text{ MW}\cdot\text{m}^{-2}\cdot\text{K}^{-1}$ ¹⁹⁻²². For the suspended configuration, thermal conductivity values between 23.2 and $84.0 \text{ W}\cdot\text{m}^{-1}\cdot\text{K}^{-1}$ are reported^{21,23,24}. These values are more accurate when averaged over large areas and were obtained by techniques with inherent limitations such as optical diffraction²⁵ in the best cases. Beyond such scales scanning thermal microscopy (SThM), developed since the 1990s²⁵ on the atomic force microscopy (AFM) platform, is attractive since the spatial resolution can depend only on the radius of the thermal contact between the probe and the sample. Such radius can reach the sub-100 nm scale under certain operation conditions, making it an option for nanoscale thermal measurements, in particular thermometry²⁶. Although SThM was already used on structures involving MoS₂ for thermometry in complex devices²⁶ and for an analysis of heat dissipation in samples where MoS₂ was coupled to graphene²⁷, it has not been used for quantitative thermal-property determination of the TMDC yet. In the present work, we propose a methodology based on ambient-condition SThM to determine the TBC value for MoS₂ monolayers grown by CVD on SiO₂/Si substrates. It is demonstrated that (in-plane) thermal conductivity is not useful in practice for samples with several microns of lateral lengths, since heat dissipation takes place towards the substrate.

The MoS₂ crystals are grown by atmospheric CVD, further details can be found in previous reports²⁸. The studied systems are composed of a MoS₂ monolayer supported by

a 300 nm-thick silica layer standing over a silicon wafer. Figure 1 shows an optical image of a typical MoS₂ monolayer, and the overall stack is reminded in the insert. The typical lateral size of the crystals is around 70-100 μm. As a large number of MoS₂ monolayers crystals (typical shapes as that of Fig. 1) can be present on the substrate, careful attention is paid to avoid thermal or optical crosstalk. Moreover, we use Raman spectroscopy to monitor the frequency difference between the E_{2g} and A_{1g} peaks⁷ to select only the single-layered MoS₂ crystals (see Suppl. Fig. 1).

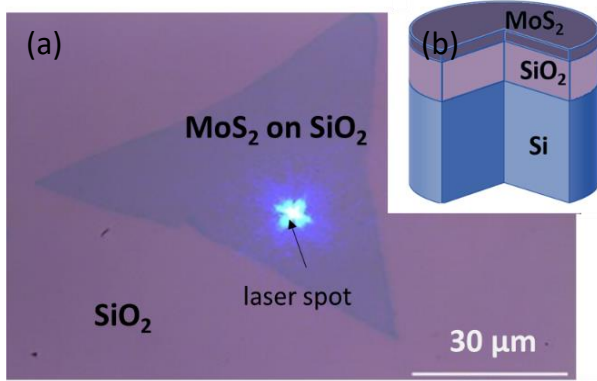


Figure 1. (a) Optical microscopy image of a MoS₂ monolayer with a triangular shape. The light dot corresponds to a laser spot irradiating the surface. (b) Cross-section schematic of the analyzed system.

Thermal scans are acquired by means of thermoresistive SThM, with two different thermal probes²⁵. The data reported here are obtained using a Wollaston probe, whose sensor is a 5 μm-in-diameter Pt₉₀/Rh₁₀ filament with a length of ≈200 μm. It is bent in a V shape with the tip contacting the sample, and anchored between unetched parts of the Wollaston wire, where the Pt₉₀/Rh₁₀ alloy is surrounded by a silver shell (≈75 μm of diameter in total). This makes the sides of the filament less electrically-resistive. As a consequence, the filament is self-heated when fed by an electrical current I . The SThM operation mode typically used in this work consists in bringing the heated probe into contact with the sample in order to heat it locally and scanning its surface at constant force as in AFM. Noticeably, the electrical resistance of the sensor R depends on the average temperature of the probe \bar{T} , so in addition to being a heat source the probe is a thermometer:

$$R = R_0 \cdot (1 + \alpha\theta), \quad (1)$$

where $\alpha = (1/R) \cdot dR/d\bar{T}$ is the temperature coefficient of the Pt₉₀/Rh₁₀ electrical resistance known to be $1.66 \times 10^{-3} \text{ K}^{-1}$, $R_0 = R(T_0)$ and $\theta = \bar{T} - T_0$ is the temperature rise above ambient temperature T_0 (see Suppl. Sec. 2 for more details on SThM). The ratio between the heat input to the sensor $P = RI^2$ and the sensor average temperature rise θ provides a qualitative estimation of the sample ability to dissipate heat, it is known as the probe thermal

conductance G_{probe} (see Suppl. Secs. 2-4) and its value is close to $95 \mu\text{W} \cdot \text{K}^{-1}$ in ambient condition.

In our setup, the current supplied to the probe is constant, and the voltage variation ΔV is monitored at the same time than the topography during the scan²⁵ of the sample surface. The voltage reference ($\Delta V = 0$) is taken at an arbitrary point on the surface. Note that thermal stabilization is reached by waiting around 45 min before scanning to minimize the impact of thermal drifts on the images. Figure 2 displays (a) the recorded AFM topography, and (b) the raw thermal image (ΔV) of a MoS₂ monolayer. It is possible to directly correlate the crystal topography (here slightly different from the crystal of Fig. 1) with the thermal contrast. One can notice the strong difference between the thermal signal on the MoS₂ monolayer and that in the region around (SiO₂/Si substrate). Artifacts linked to scan direction are observed in the topography image, and are also present in the raw thermal image.

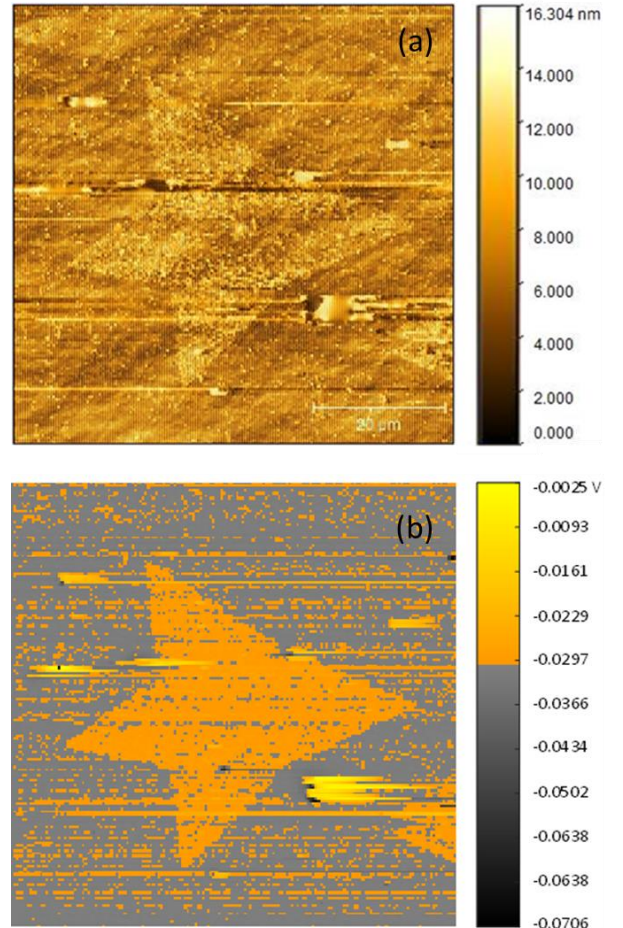


Fig 2. (a) Topography image obtained by atomic force microscopy with a Wollaston probe. A flat plane was subtracted from the raw image. (b) Raw thermal signal (ΔV) obtained during the same scan.

The raw thermal image can be translated into a probe average temperature image with Eq. (1). One obtains the

probe temperature variation $\Delta\theta$ as a function of location on the sample (with respect to some reference, here arbitrarily taken as the lowest value of the image). In order to smoothen the thermal signal fluctuations, we average the signal close to an edge as shown in Fig. 3 (the image is rotated with respect to that of Fig. 2). It is found that the probe temperature increases by approximately 0.1 K when it moves from SiO₂ to MoS₂, indicating that the MoS₂ layer induces an additional thermal resistance for the flux being dissipated into the sample. At first sight, this effect could be ascribed either to a worse contact between the SThM probe with MoS₂ than silica or to a weak thermal contact between MoS₂ and the silica. This is in striking contrast to supported graphene, which increases heat dissipation properties^{29,30}.

The temperature map is then translated into a map of the probe thermal conductance G_{probe} (again with respect to an arbitrary reference, see Suppl. Sec. 2). It is found that G_{probe} varies by $\Delta G_{\text{probe}} = 55 \times 10^{-9} \text{ W.K}^{-1}$ close to the edge of the MoS₂ crystal. It is instructive to compare this value with that obtained when simply increasing the thickness of the silica layer (silica is a standard solid-state thermal insulator). In Ref. [31], some of us reported, with a similar Wollaston SThM probe, how G_{probe} varies with SiO₂ thickness (see Suppl. Sec. 5). Assuming similar thermal conductivity for the oxide in the SiO₂/Si substrate here and that of Ref. [31], we find that the decrease of probe thermal conductance when locating the probe on MoS₂ is the same as that while bringing it over an oxide layer thicker by 95 nm. This thickness is more than hundred times than that of MoS₂, underlining the potential of the TMDC as thin but efficient heat barrier.

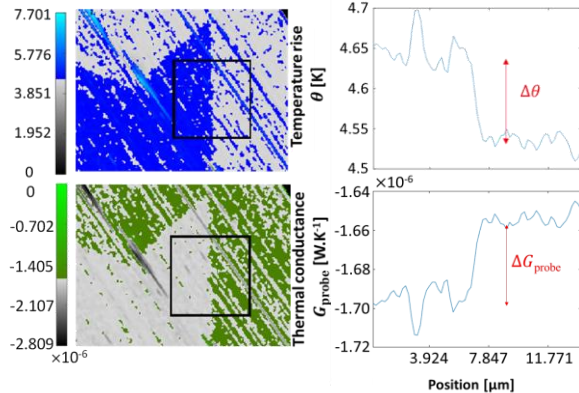


Figure 3. (Top) Probe temperature rise with respect to an arbitrary reference between the supported MoS₂ and the silica-over-silicon wafer. (Down) Probe thermal conductance deduced from the temperature measurements (arbitrary reference). Left panels show rotated images with respect to Fig. 2, and right ones vertical averages in the square for each (horizontal) position.

In the following, we aim at obtaining quantitative thermal data for the MoS₂ monolayer (see Suppl. Sec. 3 for a graphical summary of the procedure). To determine these, one needs first to find an estimate of the thermal contact radius b , i.e. the size over which the SThM probe heats the

sample. It is obtained by first comparing the probe thermal conductance with that obtained as a function of the silica thickness in Ref. [31]. The effective thermal conductivity (that of a bulk leading to the same G_{probe}) determined for a layer of 300 nm of SiO₂ over Si is around $\lambda_{\text{eff}} \approx 2 \text{ W.m}^{-2}.\text{K}^{-1}$ (see Suppl. Sec. 6). The radius can then be obtained from a finite element (FE) simulation solving the steady-state heat equation, in the sample only. Indeed, the sample thermal conductance (conductance associated with heat dissipation in the sample from a hot isothermal disc on the sample surface) is $4\lambda_{\text{eff}}b$ and equal to that of the exact geometry (300 nm SiO₂/Si) for an identical thermal contact radius. The radius determined from the FE simulation is around 4 μm (see Suppl. Sec. 7 for more details). This value underlines the well-known fact that heat spreads from the probe to the sample in the air, leading to a transfer over a much larger area than that of the mechanical contact²⁵. Since heat is transferred mostly through air to the sample, the thermal boundary conductance at the mechanical contact is not a matter of concern. Note that the impact of the thermal contact conductance between the tip and the sample depends only on the effective (bulk) thermal conductivity felt by the probe for heat transfer through air³². This is in stark contrast to many works where heat transfer inside the whole system made of the SThM sensor and at the probe-sample contact is also required to be modelled. This simplification is possible because the current work builds on the previous calibration in Ref. [31].

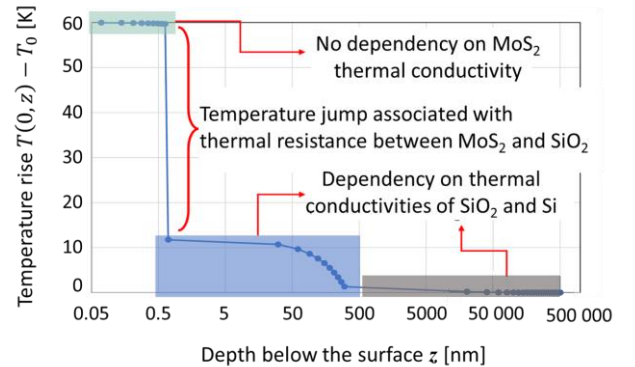


Figure 4. Temperature profile in logarithmic scale as a function of depth below the heat source (FEM simulation). The upper region overlaid in green corresponds to the MoS₂ monolayer, the lower blue region corresponds to SiO₂, and, finally, the gray region corresponds to the contribution of the Si substrate.

The final step is also performed with a FE simulation. The actual geometry, i.e. the stack shown in the inset of Fig. 1, is considered, with known thermal conductivity values for silicon and silica, and again with a disc of homogeneous temperature as heat input on the top (see Suppl. Sec. 8). The unknowns are the MoS₂ thermal conductivity, supposed isotropic in the 0.7 nm thickness, and the TBC between MoS₂ and silica. These two quantities are adjusted in the 2D cylindrical FE simulation to dissipate a power equivalent to that of a bulk with the effective

thermal conductivity mentioned above (i.e. the bulk and MoS₂/SiO₂/Si sample thermal conductances are equal). It is found that the value of the thermal conductivity of MoS₂ impacts very weakly the temperature distribution, which is driven only by the TBC. The temperature profile in the center of the structure is provided in Fig. 4 as a function of depth. Note that we verified that the MoS₂ lateral size and shape do not matter provided that the size is larger than the thermal contact radius. The temperature profile is mostly flat in the thin TMDC layer (see Suppl. Fig. 8 for 3D temperature distribution), as a result of the insensitivity to thermal conductivity. Most importantly, there is a strong temperature discontinuity associated with the MoS₂/SiO₂ interface. Finally, one obtains a value of $4.6 \pm 2 \text{ MW.m}^{-2}.\text{K}^{-1}$ for the thermal boundary conductance, which is close to the values found experimentally for flakes by Raman thermometry^{12,20} and of similar order of magnitude to a molecular dynamic study³³. The value is intrinsically low as Van Der Waals bonding provides a much weaker connection between the monolayer and its support. It seems therefore that the quality of the material, being it an exfoliated flake or a CVD-grown crystal, is not key for heat conduction when it is supported.

In summary, this work has shown that, with a proper calibration technique, SThM allows for quantitative determination of key parameters associated with heat dissipation in supported 2D materials. Thermal conductivity may not be the relevant parameter, while Van Der Waals bonding leads to weak thermal coupling with substrates. In the near future, it will be useful to analyze TMDCs with a better spatial resolution, either by studying the jump at contact in probe approach curves or by implementing vacuum conditions. Analyzing heat dissipation in TMDCs as a function of temperature may also enable to discriminate between the effect of thermal conductivity and thermal boundary conductance²⁷.

See the Supplementary Information for details on material, the temperature-probe thermal conductance connection, for details on the varying-thickness oxide calibration samples and on the simulations.

We thank J.-M. Bluet for helping with the Raman characterization and A. Alkurdi for discussions. C.M.F.A. acknowledges a CONACYT scholarship funding. S.G. and P.-O.C. acknowledge support of project TIPTOP (ANR-16-CE09-0023) and A.D.L.B. the support of project UNAM-PAPIIT-A101822.

References

- ¹ R. Peköz, M. Konuk, M.E. Kilic, and E. Durgun, *ACS Omega* **3**, 1815 (2018).
- ² T. Knobloch, Y.Y. Illarionov, F. Ducry, C. Schleich, S. Wachter, K. Watanabe, T. Taniguchi, T. Mueller, M. Walzl, and M. Lanza, *Nat. Electron.* **4**, 98 (2021).
- ³ L.M. Xie, *Nanoscale* **7**, 18392 (2015).

- ⁴ I.D. Marion, D. Čapeta, B. Pielic, F. Faraguna, A. Gallardo, P. Pou, B. Biel, N. Vujicic, and M. Kralj, *Nanotechnology* **29**, 305703 (2018).
- ⁵ Y. Lee, X. Zhang, W. Zhang, M. Chang, C. Lin, K. Chang, Y. Yu, J.T. Wang, C. Chang, and L. Li, *Adv. Mater.* **24**, 2320 (2012).
- ⁶ P. Yang, S. Zhang, S. Pan, B. Tang, Y. Liang, X. Zhao, Z. Zhang, J. Shi, Y. Huan, and Y. Shi, *ACS Nano* **14**, 5036 (2020).
- ⁷ S. Ganorkar, J. Kim, Y.-H. Kim, and S.-I. Kim, *J. Phys. Chem. Solids* **87**, 32 (2015).
- ⁸ K.M. McCreary, E.D. Cobas, A.T. Hanbicki, M.R. Rosenberger, H.-J. Chuang, S. V Sivaram, V.P. Oleshko, and B.T. Jonker, *ACS Appl. Mater. Interfaces* **12**, 9580 (2020).
- ⁹ G. Deokar, D. Vignaud, R. Arenal, P. Louette, and J.-F. Colomer, *Nanotechnology* **27**, 75604 (2016).
- ¹⁰ D.P. Rai, T. V Vu, A. Laref, M.P. Ghimire, P.K. Patra, and S. Srivastava, *Nano-Structures & Nano-Objects* **21**, 100404 (2020).
- ¹¹ P. Ni, A. De Luna Bugallo, V.M. Arellano Arreola, M.F. Salazar, E. Strupiechonski, V. Brandli, R. Sawant, B. Alloing, and P. Genevet, *ACS Photonics* **6**, 1594 (2019).
- ¹² F. Xia, H. Wang, D. Xiao, M. Dubey, and A. Ramasubramaniam, *Nat. Photonics* **8**, 899 (2014).
- ¹³ D.G. Cahill, *Rev. Sci. Instrum.* **61**, 802 (1990).
- ¹⁴ A. Abareshi, M. Arshadi Pirlar, and M. Houshiar, *Mater. Res. Express* (2019).
- ¹⁵ E. Yalon, Ö.B. Aslan, K.K.H. Smithe, C.J. McClellan, S. V Suryavanshi, F. Xiong, A. Sood, C.M. Neumann, X. Xu, K.E. Goodson, T.F. Heinz, and E. Pop, *ACS Appl. Mater. Interfaces* **9**, 43013 (2017).
- ¹⁶ T. Tong and A. Majumdar, *Rev. Sci. Instrum.* **77**, 104902 (2006).
- ¹⁷ P. Jiang, X. Qian, X. Gu, and R. Yang, *Adv. Mater.* **29**, 1701068 (2017).
- ¹⁸ S. Shree, A. George, T. Lehnert, C. Neumann, M. Benelajla, C. Robert, X. Marie, K. Watanabe, T. Taniguchi, U. Kaiser, B. Urbaszek, and A. Turchanin, *2D Mater.* **7**, 15011 (2019).
- ¹⁹ S. Sahoo, A.P.S. Gaur, M. Ahmadi, M.J.-F. Guinel, and R.S. Katiyar, *J. Phys. Chem. C* **117**, 9042 (2013).
- ²⁰ A. Taube, J. Judek, A. Łapińska, and M. Zdrojek, *ACS Appl. Mater. Interfaces* **7**, 5061 (2015).
- ²¹ X. Zhang, D. Sun, Y. Li, G.-H. Lee, X. Cui, D. Chenet, Y. You, T.F. Heinz, and J.C. Hone, *ACS Appl. Mater. Interfaces* **7**, 25923 (2015).
- ²² J. Judek, A.P. Gertych, M. Świniarski, A. Łapińska, A. Dużyńska, and M. Zdrojek, *Sci. Rep.* **5**, 1 (2015).
- ²³ A.J. Gabourie, S. V. Suryavanshi, A.B. Farimani, and E. Pop, *2D Mater.* **8**, 11001 (2021).
- ²⁴ R. Yan, J.R. Simpson, S. Bertolazzi, J. Brivio, M. Watson, X. Wu, A. Kis, T. Luo, A.R. Hight Walker, and H.G. Xing, *ACS Nano* **8**, 986 (2014).
- ²⁵ S. Gomès, A. Assy, and P.O. Chapuis, *Phys. Status Solidi Appl. Mater. Sci.* **212**, 477 (2015).
- ²⁶ S. Vaziri, E. Yalon, M.M. Rojo, S. V. Suryavanshi, H. Zhang, C.J. McClellan, C.S. Bailey, K.K.H. Smithe, A.J. Gabourie, V. Chen, S. Deshmukh, L. Bendersky, A. V. Davydov, and E. Pop, *Sci. Adv.* **5**, 1 (2019).
- ²⁷ C. Evangeli, J. Spiece, S. Sangtarash, A.J. Molina-Mendoza, M. Mucientes, T. Mueller, C. Lambert, H. Sadeghi, and O. Kolosov, *Adv. Electron. Mater.* **5**, 1 (2019).
- ²⁸ V.M.A. Arreola, M.F. Salazar, T. Zhang, K. Wang, A.H.B. Aguilar, K.C.S. Reddy, E. Strupiechonski, M. Terrones, and A.D.L. Bugallo, *2D Mater.* **8**, 25033 (2021).
- ²⁹ F. Menges, H. Riel, A. Stemmer, C. Dimitrakopoulos, and B. Gotsmann, *Phys. Rev. Lett.* **111**, 205901 (2013).
- ³⁰ M.E. Pumarol, M.C. Rosamond, P. Tovee, M.C. Petty, D.A.

Zeze, V. Falko, and O. V Kolosov, *Nano Lett.* **12**, 2906 (2012).

³¹ E. Guen, P.-O. Chapuis, R. Rajkumar, P.S. Dobson, J.M.R. Weaver, and S. Gomes, *J. Appl. Phys.* **128**, 235301 (2020).

³² A.M. Massoud, J.-M. Bluet, V. Lacatena, M. Haras, J.-F. Robillard, and P.-O. Chapuis, *Appl. Phys. Lett.* **111**, 63106 (2017).

³³ Z.-Y. Ong, Y. Cai, G. Zhang, and Y.-W. Zhang, *Nanotechnology* **32**, 135402 (2021).

SUPPLEMENTARY MATERIAL TO

Thermal boundary conductance of CVD-grown MoS₂ monolayer-on-silica substrate determined by scanning thermal microscopy

C.M. Frausto-Avila^{a,b}, V. Arellano-Arreola^b, J.M. Yañez-Limon^b, A. De Luna-Bugallo^b, S. Gomès^a, P.-O. Chapuis^a

^a Univ Lyon, CNRS, INSA-Lyon, Université Claude Bernard Lyon 1, CETHIL UMR5008, F-69621, Villeurbanne, France.

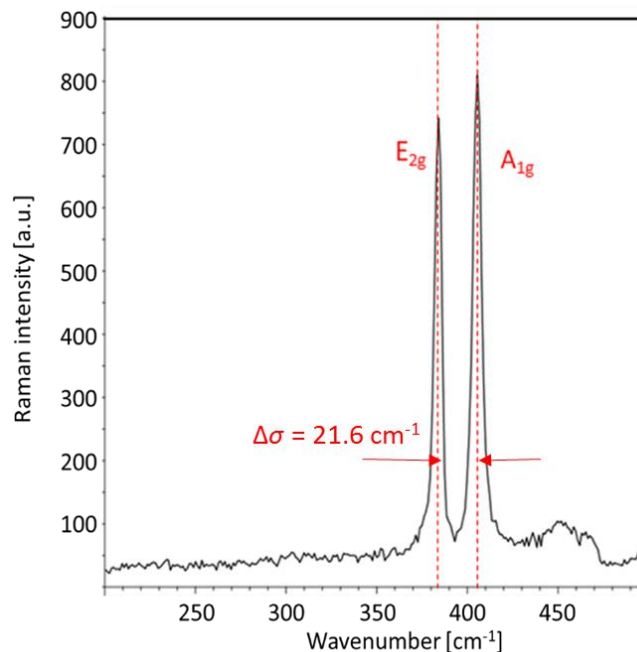
^b Cinvestav Unidad Querétaro, Querétaro, Qro. 76230, Mexico

Contents

1. Procedure to determine if the sample is a MoS₂ monolayer
2. Procedure to determine the probe thermal conductance
3. Brief summary of the different steps for the data treatment
4. Thermal circuit associated to heat dissipation from the probe
5. 'Equivalent oxide thickness' procedure
6. Equivalent effective thermal conductivity
7. Determination of the thermal contact radius
8. Determination of the thermal boundary conductance

1. Procedure to determine if the sample is a MoS₂ monolayer

According to the methodology followed by Ganorkar *et al.*¹ for estimating the number of MoS₂ layers synthesized by Chemical Vapor Deposition (CVD), the difference between the Raman shifts of the E_{2g} and A_{1g} peaks is used to estimate the number of layers. The wavenumber difference is $\Delta\sigma = 21.5 \text{ cm}^{-1}$ for a monolayer and $\Delta\sigma = 22.3 \text{ cm}^{-1}$ for bilayers [1]. In this work we find a value of $\Delta\sigma = 21.6 \text{ cm}^{-1}$, which can safely be considered as a MoS₂ monolayer crystal (see Suppl. Fig. 1).



Suppl. Fig. 1. MoS₂ Raman spectrum.

2. Procedure to determine the probe thermal conductance

The probe thermal conductance is defined as

$$G_{probe} = P/\theta, \quad (1)$$

where $P = R I^2$ is the Joule self-heating power inside the sensitive part (sensor) of the probe, R the electrical resistance of the sensitive part of the probe (sensor), I is the electrical current in the probe and θ its mean temperature rise with respect to ambient. The Wollaston probe resistance is inserted into a Wheatstone bridge (see Suppl. Fig. 2), and it is the bridge imbalance voltage ΔV that is provided in the thermal image. As a result, scans provide only temperature rises

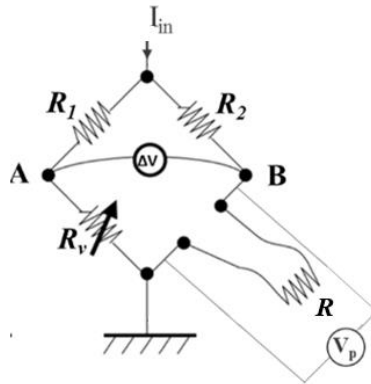
$$\Delta\theta = \frac{\Delta V}{I} \cdot \frac{1}{\alpha R} \quad (2)$$

relative to an absolute reference temperature $\theta_{ref} + T_0$, which is selected by balancing the bridge ($\Delta V = 0$), and not directly the probe voltage V_p . It is customary to balance the bridge either far from contact ($\theta_{ref} = \bar{T} - T_0$, where \bar{T} is the average temperature in the sensor), or in contact at a given location on the sample ($\theta_{ref} = \bar{T} - T_{ref}$). Here, the second option is chosen.

Knowing the value of the electrical resistance in the bridge R_v , one can deduce the probe temperature $T_0 + \theta = T_0 + \theta_{ref} + \Delta\theta$. We use a symmetric bridge, so that $R_1 = R_2$ (taken as 50Ω), and an input bridge current of $I_{in} = 80$ mA, i.e. $I = 40$ mA is supplied in the probe. The electrical resistance of the sensitive part of the Wollaston probe (Pt₉₀/Rh₁₀ filament) R is computed by determining the geometrical parameters, noticing that the variable resistance, when the bridge is balanced, is equal to:

$$R_v = R_{wiring} + R_{Ag} + R, \quad (3)$$

where the electrical resistance of the wiring is estimated to be $R_{wire} \approx 1 \Omega$, $R = R_0(1 + \alpha(\theta))$ and R_{Ag} is obtained by subtraction from room-temperature measurements ($\theta = 0$). R_{Ag} is the electrical resistance of the Wollaston wire (cantilever) assumed made of the silver shell.



Suppl. Fig. 2. Wheatstone bridge where R_1 and R_2 , R_v and R are the fixed electrical resistances, the variable electrical resistance and the electrical resistance of the probe respectively.

The local probe thermal conductance variation is obtained as in Ref. [2] by differentiating logarithmically Eq. (1), which gives after straightforward algebra:

$$\Delta G_{probe} = G_{probe} - G_{probe ref} = G_{probe ref} \cdot \Delta\theta \cdot \left[\alpha(\theta) - \frac{1}{\theta} \right] \quad (4)$$

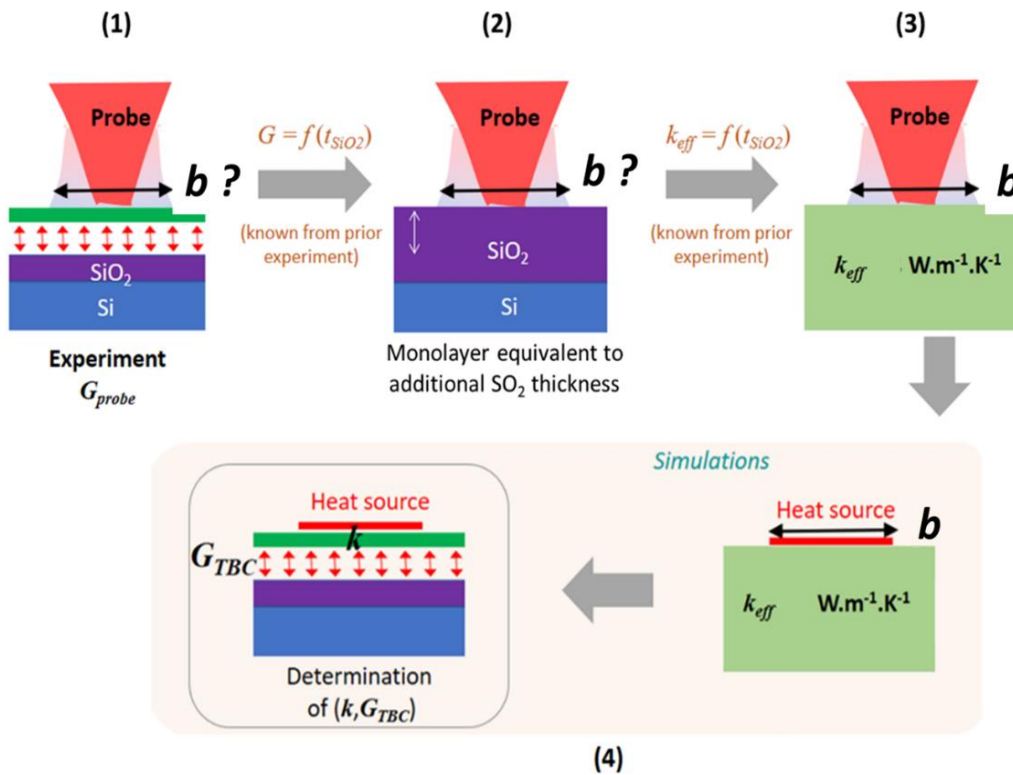
if the current variation in the probe ΔI is neglected (which we verified). $G_{probe ref}$ is the probe thermal conductance at absolute temperature $T_0 + \theta_{ref}$. Of course Eq. (4) is valid only provided the thermal conductance variations stay small. A direct calculation without linearization can be performed if this is not the case.

From the parameters experimentally determined, $G_{probe 0} \approx 95 \mu\text{W} \cdot \text{K}^{-1}$ and $\theta_{ffc} \approx 156$ K far from contact. When the probe contacts the sample, the temperature rise θ decreases by about 10% for materials of moderate thermal conductivities, so $\theta_{ref} \approx 140$ K. In principle $G_{probe ref}$ and $G_{probe 0}$ are different, but in the following Eq. (4) is used with the assumption $G_{probe ref} \approx G_{probe 0}$, which induces an uncertainty propagation in ΔG_{probe} . Note that maps of ΔG_{probe} or G_{probe} with respect to an arbitrary reference provide similar information.

3. Brief summary of the different steps for the data treatment

The raw SThM image allows only acquiring qualitative analysis of heat dissipation at the sample surface and a significant part of the work is therefore to deduce quantitative data from these images. We summarize the different steps (see Suppl. Fig. 3) mentioned in the main manuscript here, and more details are provided in the Sections below.

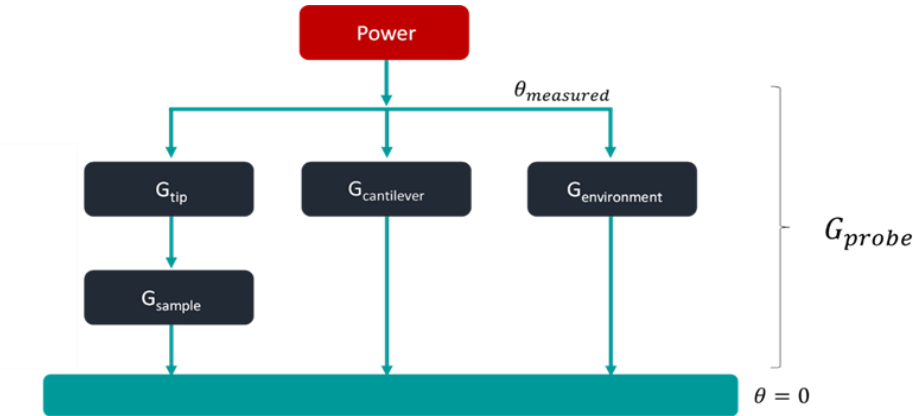
- First (1), the local probe thermal conductance G_{probe} is obtained from the electrical data (see above).
- Then (2), the calibration from Guen *et al.* [3] allows obtaining an oxide thickness that impacts the probe thermal conductance equivalently as MoS₂. This step is interesting for qualitative reasoning but not decisive for the following.
- More importantly (3), the same paper [3] allows determining the two effective bulk thermal conductivities k_{eff} that provide the same probe thermal conductance as that of the MoS₂/SiO₂/Si and the SiO₂/Si samples, respectively. Noticeably, all the previous steps do not require simulations. But they do not allow to determine the thermal contact radius b .
- The simulation steps (4) involve Finite Element (FE) modelling. We proceed in two steps: (4a) we first determine the thermal contact radius b , and then (4b) we use it to determine the MoS₂ thermal properties. The thermal radius is obtained by equating the thermal conductances of the effective bulk geometry (known to be $G_{sample} = 4k_{eff}b$) and of the exact SiO₂/Si geometry. Then for such radius a FE simulation of the MoS₂/SiO₂/Si stack is performed. The thermal conductivity of the monolayer k and the thermal boundary conductance between the monolayer and the supporting material G_{TBC} are varied in order to match the stack effective thermal conductivity determined in (3).



Suppl. Fig. 3. Schematic of the different steps of our approach for quantitative measurement.

4. Thermal circuit associated to heat dissipation from the probe

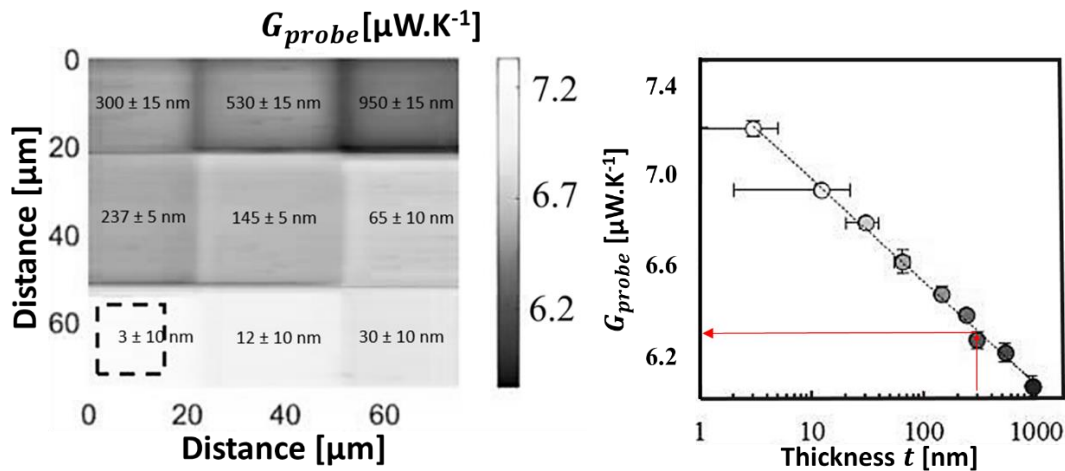
We provide a schematic clarifying the different thermal conductances involved in our SThM experiments. G_{probe} is in principle indeed the sum of the three channels allowing heat to dissipate from the probe, where only one is useful for the experiment. However $G_{environment} \approx 0$ when the probe is in contact³. G_{tip} includes the thermal contact conductance associated with the transport of heat from the tip into the sample, and is usually difficult to determine precisely. The method described below (Suppl. Sec. 5) avoids addressing this issue fully.



Suppl. Fig. 4. Suppl. Fig. 3. Thermal circuit associated with heat dissipation in the probe.

5. ‘Equivalent oxide thickness’ procedure (Step (2) of Suppl. Fig. 3)

To find the equivalent thickness of SiO_2 that induces a similar thermal resistance in the sample as that of the monolayer of MoS_2 , we use a calibration sample³ made of a mosaic of silicon oxide layers with different thicknesses coating a silicon wafer. It happens that the substrate below MoS_2 is similar, with a SiO_2 layer on top of the silicon wafer. Since the two samples were not prepared at the same time and with the same goal, some uncertainty is introduced by comparing the data, which propagates until the determination of the thermal boundary conductance. The calibration sample is shown in Suppl. Fig. 5 and detailed in the previous publication³ (beware that notations are not the same and that the probe thermal conductance defined here is based on the probe average temperature, not the probe apex one).

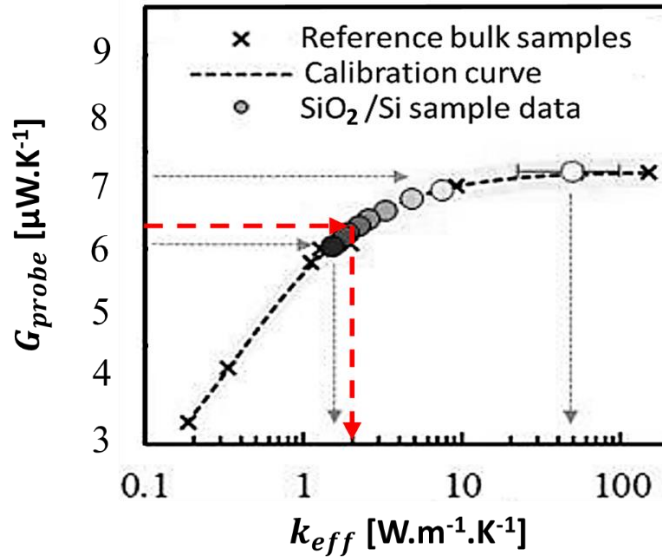


Suppl. Fig. 5. (Left) SThM scan of the mosaic sample made of 9 different thicknesses of silica. The heights of the silicon oxide steps are indicated on the images. (Right) Probe thermal conductance for the different SiO_2 thicknesses. The probe thermal conductance reference ($G_{probe} = 0$) is the far-from-contact position.

More precisely, G_{probe} varies of $\Delta G_{probe} = 55 \times 10^{-9} \text{ W.K}^{-1}$ when the probe moves from the MoS_2 crystal to the oxide surface (see Fig. 3 in the main paper). Note that $\Delta G_{probe} = G_{probe}(\text{MoS}_2) - G_{probe}(\text{SiO}_2 \text{ 300 nm})$. From Suppl. Fig. 5, we find that $G_{probe}(\text{SiO}_2 \text{ 300 nm}) + \Delta G_{probe} = G_{probe}(\text{SiO}_2 \text{ 395nm})$ in the calibration sample.

6. Equivalent effective thermal conductivity (Step (3) of Suppl. Fig. 3)

The effective thermal conductance for the {oxide on silicon} sample is obtained from the calibration curve in Ref. [3], as shown in Suppl. Fig. 6. The advantage of this method is that it provides a quantity that depends only on the sample and does not require the knowledge of the thermal conductance corresponding to the heat transfer between the probe and the sample included in G_{tip} . For the value of G_{probe} found in Suppl. Fig. 5, we find $k_{eff} \approx 2.1 \text{ W.m}^{-1}.\text{K}^{-1}$ in Suppl. Fig. 5.



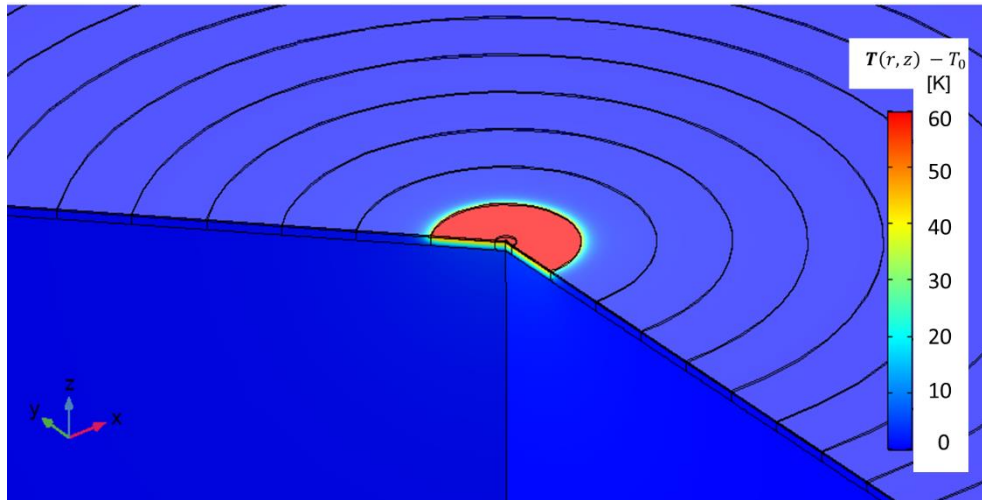
Suppl. Fig. 6. Variation of the probe thermal conductance (reference far from contact) as a function of the effective thermal conductivity.

7. Determination of the thermal contact radius

The thermal contact radius, i.e. the size of the hot zone on the sample surface (assumed to be a disc), is required for the final step. One can consider that there is a single thermal contact radius for each effective thermal conductivity, i.e. the radius does not depend on the exact configuration within the sample but only on the thermal conductance G_{sample} ⁴. This conductance is not known initially, and we are required to perform simulations in order determine the thermal contact radius for the {silica on silicon} sample.

With finite-element (FE) simulations, we compute the thermal conductance of a medium consisting of a silica layer (300 nm) over a silicon wafer, for a given radius (see Suppl. Fig. 7). This can be done for an arbitrary temperature on the top T_{top} of the simulated sample provided the thermal conductivities are considered temperature-independent. The lateral and bottom sides of the domain are considered at a fixed ambient temperature $T_{ambient}$. The sample thermal conductance within such geometry $G_{sample} = Q/(T_{top} - T_{ambient})$ is computed and compared to the conductance associated with the effective thermal conductivity, known analytically to be $G_{sample} = 4k_{eff}b$ (defined as that of an equivalent-bulk thermal conductance for the same radius), determined from Suppl. Fig. 6. When the two thermal conductances are equal, this process provides the thermal contact radius b . We find $b \approx 4 \mu\text{m}$, which confirms that air heat transfer predominates.

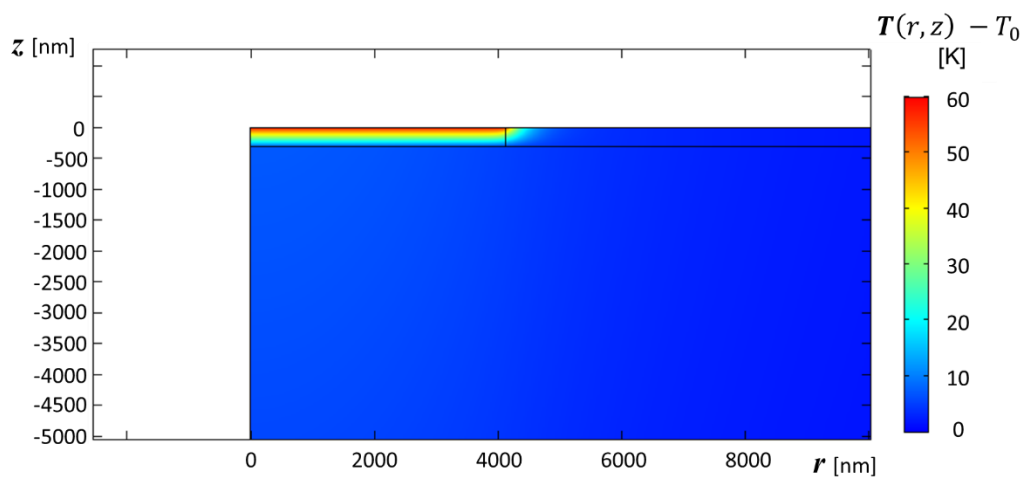
This work can also be performed for a 395-nm silicon oxide layer, which provides the equivalent sample thermal conductance as that of the MoS₂/SiO₂/Si system. Note that we do not consider here possible partially-ballistic dissipation in contrast to Ref. [4].



Suppl. Fig. 7. Temperature distribution on the equivalent (395 nm SiO₂ film on Si substrate) sample surface.

8. Determination of the thermal boundary conductance

In the final step, we perform simulations with the thermal radius previously determined by varying the thermal conductivity of MoS₂ k and the thermal boundary conductances G_{TBC} at its boundary with SiO₂. While the values of thermal conductivity k do not impact much on the total sample thermal conductance (which is known to be $4k_{eff}b$, where b is the thermal radius), one value of the boundary conductance provides the correct sample thermal conductance. The cross section temperature field is shown in Suppl. Fig. 8, and as a function of depth z on the revolution axis in the core paper.



Suppl. Fig. 8. Temperature field in a cross section of the MoS₂/SiO₂/Si sample.

References

1. Ganorkar, S., Kim, J., Kim, Y.-H. & Kim, S.-I., Effect of precursor on growth and morphology of MoS₂ monolayer and multilayer, *J. Phys. Chem. Solids* 87, 32–37 (2015).
2. Lucchesi, C., Cakiroglu, D., Perez, J.-P., Talercio, T., Tournié, E., Chapuis, P.-O., Vaillon, R., Near-field thermophotovoltaic conversion with high electrical power density and cell efficiency above 14%, *Nano Letters* 21, 4524 (2021).
3. Guen, E., Chapuis, P.-O., Rajkumar, R., Dobson, P.S., Weaver, J.M.R., Gomès, S., Scanning thermal microscopy probes using a sample of varying thermal conductivities with identical surfaces, *Journal of Applied Physics* 128, 235301 (2020)
4. Massoud, A. M., Bluet, J.-M., Lacatena, V., Haras, M., Robillard, J.-F., Chapuis, P.-O., Native oxide limited thermal transport in suspended silicon membrane revealed by scanning thermal microscopy, *Applied Physics Letters* 111, 063106 (2017)